




# Automated Grain Yield Behavior Classification

DARREN C. PAGAN <sup>1,5</sup> JAKOB KAMINSKY,<sup>1,2</sup> WESLEY A. TAYON,<sup>3</sup>  
KELLY E. NYGREN,<sup>1</sup> ARMAND J. BEAUDOIN,<sup>1,4</sup>  
and AUSTIN R. BENSON<sup>2</sup>

1.—Cornell High Energy Synchrotron Source, Cornell University, Ithaca, NY 14853, USA. 2.—Department of Computer Science, Cornell University, Ithaca, NY 14853, USA. 3.—NASA Langley Research Center, Hampton, VA 23666, USA. 4.—Department of Mechanical Science and Engineering, University of Illinois at Urbana-Champaign, Urbana, IL 61801, USA. 5.—e-mail: dcp99@cornell.edu

A method for classifying grain stress evolution behaviors using unsupervised learning techniques is presented. The method is applied to analyze grain stress histories measured in situ using high-energy x-ray diffraction microscopy from the aluminum–lithium alloy Al-Li 2099 at the elastic–plastic transition (yield). The unsupervised learning process automatically classified the grain stress histories into four groups: major softening, no work-hardening or -softening, moderate work-hardening, and major work-hardening. The orientation and spatial dependence of these four groups are discussed. In addition, the generality of the classification process to other samples is explored.

## INTRODUCTION

The macroscopic constitutive response and failure criteria of engineering alloys are dictated by the behaviors of the individual grains that comprise the material. To understand these behaviors, experimental characterization techniques have advanced to simultaneously measure the in situ micromechanical response of many individual grains, both on the surface of samples in a scanning electron microscope<sup>1–3</sup> and in the bulk of samples using x-ray techniques.<sup>4</sup> A natural challenge that arises once these data have been collected is how to efficiently extract critical information about the constitutive response. Previous research using these large datasets has tended to the extremes: analyzing a handful of grains in great detail<sup>5–9</sup> or averaging over the entire collection of grains probed.<sup>10–12</sup> Driving these extremes are the limitations imposed by manual analysis. Instead, we propose the use of unsupervised learning techniques to distill the ensemble behavior of *all* grains probed down to fundamental descriptors. In this work, we demonstrate the utility of this approach by analyzing the tensile deformation behavior of  $\approx 100$  grains in the aluminum–lithium alloy Al-Li 2099 through the elastic–plastic transition (yield).

The application of machine learning to materials science has been proposed as a path forward for attaining new insights into engineering alloy behavior and guiding the creation of new alloy systems.<sup>13</sup> A great deal of focus has been placed on building new tools to link structure and properties in an automated fashion in order to accelerate the materials design process.<sup>14–18</sup> However, as mentioned, other challenges exist regarding the interpretation and analysis of the large datasets that we can now gather using electron microscopes, synchrotron x-ray and neutron facilities, and large-scale numerical models. With these ‘big data’, it can now be difficult to simply determine *what features are important in a dataset*. Other researchers have begun to attempt to address the challenge by developing new methods to find critical deformation behaviors in large datasets and to tie these to microstructural features.<sup>19–21</sup> Likewise, we present a new method for classifying yield behavior from grain stress histories in individual grains (which can presently be both measured and modeled) using the unsupervised learning techniques of principal component analysis and clustering.

This paper will analyze grain stress data from the Al-Li 2099 alloy, which has been previously studied using more traditional methods, to unpack the constituent grain stress behaviors.<sup>22</sup> Al-Li alloys

## MATERIALS AND METHODS

offer increased specific stiffness and strength, compared to conventional aluminum alloys, making them attractive for use in aerospace and spaceflight applications. However, these alloys are also susceptible to grain boundary cracking (known as delamination fracture)<sup>23</sup> that has been attributed to specific grain pairings.<sup>24</sup> The former study investigated these mechanisms through the manual inspection of individual grain stress responses measured in situ using high-energy x-ray diffraction microscopy (HEDM) during uniaxial tension. In the study, two clear grain stress behaviors could be identified: a decrease in flow stress at yield (softening) and continuous increases in flow stress (work-hardening). As examples, Fig. 1 shows the evolution of the normal stress components along the loading direction  $\sigma_{yy}$  with increasing macroscopic strain  $\varepsilon$  for representative grains of the two behaviors. It was observed that the grains that soften initially (display a yield point) were often oriented primarily for crystallographic slip on a single slip system, while hardening grains were oriented for polyslip. However, challenges still existed classifying the behavior of grains whose behaviors were between the extremes, such as the response also shown in Fig. 1. As will be shown, unsupervised learning can aid classification of all grains probed. With behaviors properly grouped, unifying microstructural characteristics can be determined for the development of constitutive relationships and state evolution equations.

The outline of the paper is as follows. The “Materials and Methods” section will briefly review data collection and focus on processing of the grain stress data. The “Results and Analysis” section will present results regarding the classification of yield behavior in Al-Li 2099 grains. The results will be discussed and physically interpreted in the “Discussion” section, while a summary will be provided in the “Summary” section.

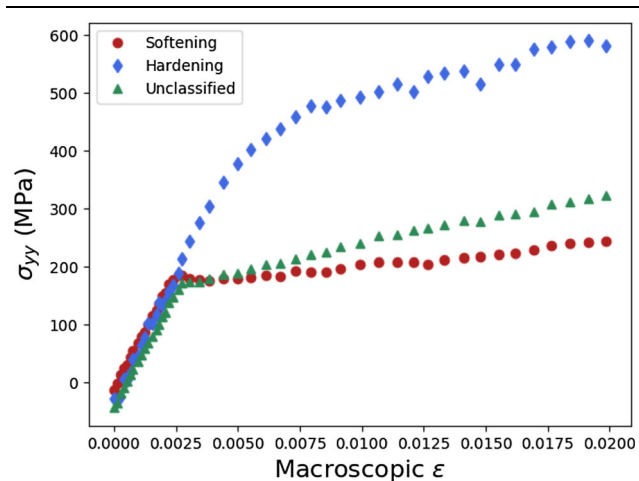


Fig. 1. Example histories of the stress evolution along the loading direction ( $\sigma_{yy}$ ) from Al-Li 2099 measured using far-field HEDM during in situ uniaxial tension. Shown are examples of softening, hardening, and unclassified stress evolution behavior.

The data collection and stress calculations are described in more detail in Ref. 22, but a short summary follows. An Al-Li 2099 specimen was deformed in uniaxial tension in displacement control at a rate of 10 nm/s to a final engineering strain of 0.02. Prior to loading, the 3-dimensional grain morphology was characterized using the box-beam near-field HEDM technique.<sup>25,26</sup> As the sample was loaded, far-field HEDM scans were performed continuously from which elastic strain tensors<sup>27</sup> of 110 grains were found at each scan. For analysis, only grains with high confidence in the data were used (completeness  $>0.9$  and  $\chi^2 < 0.005$ <sup>27</sup>), leaving 76 grains. With scan lengths of approximately 5 min, strain tensors from the grain set were measured at 21 points in the elastic regime and 27 points in the plastic regime. The average stress in each grain was then determined by evaluating the anisotropic form of Hooke’s Law. Single-crystal moduli used were (in GPa)  $C_{11} = 110$ ,  $C_{12} = 58$ , and  $C_{44} = 30$ . Lastly, to facilitate analysis of crystallographic slip behavior, the maximum resolved shear stress (mRSS,  $\tau_M$ ) applied to the 12  $[110]\langle 111 \rangle$  FCC slip systems at each measurement was calculated:

$$\tau_M = \max(\boldsymbol{\sigma} : (\mathbf{s} \otimes \mathbf{n})). \quad (1)$$

In total, at the end of data collection and this processing, the evolution of mRSS as a function of macroscopic strain  $\varepsilon$  for all grains probed was attained.

To improve the efficacy of the unsupervised behavior classification, the mRSS data  $\tau_M$  were denoised using total variation regularization.<sup>28,29</sup> Denoised mRSS histories  $\tau_{M'}$  were found by minimizing the function:

$$\int_{\varepsilon_I}^{\varepsilon_F} |d\tau_{M'}| d\varepsilon + \frac{\lambda}{2} \int_{\varepsilon_I}^{\varepsilon_F} (\tau_{M'} - \tau_M)^2 d\varepsilon \quad (2)$$

where  $\varepsilon_I$  and  $\varepsilon_F$  are initial and final strains. The penalty term  $\lambda$  provides a trade-off in the minimization between regularization of the data (the first term in Eq. 2) and data fidelity (the second term in Eq. 2). A value of  $\lambda = 5 \times 10^6$  was selected for this work. An example of raw data versus denoised data is shown in Fig. 2, from which it can be seen that the critical behaviors such as softening are still captured, but the point-to-point variation has been reduced. In addition, to focus on the grain behavior at yield,  $\varepsilon_I$  and  $\varepsilon_F$  were chosen to be 0.002 and 0.008, respectively, resulting in a time history of 16 values for each grain. The inset of Fig. 2 shows an example truncated mRSS history.

With the mRSS histories cleaned and extracted, data from the high confidence grains were processed using principal component analysis (PCA) in the usual manner.<sup>30</sup> A data matrix  $[X]$  was assembled with each row consisting of a  $\tau_{M'}$  history

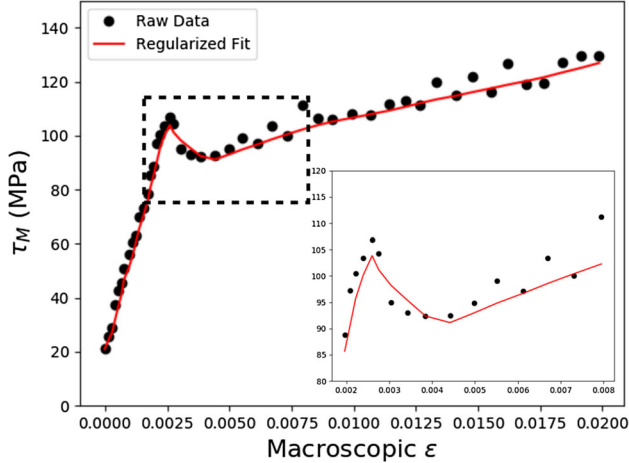


Fig. 2. An example of raw and denoised mRSS history ( $\tau_M$  and  $\tau_M$ ). Inset reduced subset of the mRSS data used in principal component analysis.

$$[X] = \begin{bmatrix} \{\tau_M^1\}^T \\ \{\tau_M^2\}^T \\ \vdots \\ \{\tau_M^n\}^T \end{bmatrix}, \quad (3)$$

creating a  $76 \times 16$  matrix. The data matrix columns were then normalized such that the mean of each column was equal to 0 to create  $[\tilde{X}]$ . In this organization of the mRSS data, each grain stress history serves as an independent observation. Principal component vectors  $\{w^j\}$  were then calculated as the eigenvectors of  $[\tilde{X}]^T[\tilde{X}]$ . The first three principal component vectors were used to calculate scores  $z$  for each grain history with a score defined as:

$$z^j = \{w^j\} \cdot \{\tau_M^i\}. \quad (4)$$

For the dataset analyzed, 71.2%, 98.0%, and 99.8% of the data variance are explained by use of one, two, and three principal component vectors, respectively, while inclusion of a fourth principal component vector increases the explained data variance to 99.9%. Once scores for each grain stress history were found, the grain behaviors were clustered using the K-Means algorithm.<sup>30</sup> The optimum number of clusters was determined by adding clusters until diminishing returns were gained in the cost function.

## RESULTS AND ANALYSIS

The first three principal component vectors  $\{w^j\}$  are plotted versus macroscopic strain in Fig. 3, with the principal vectors labeled A–C. We note that the principal vectors are only unique to sign, and the signs of each vector as plotted and used were chosen to facilitate comparison to the mRSS histories. We

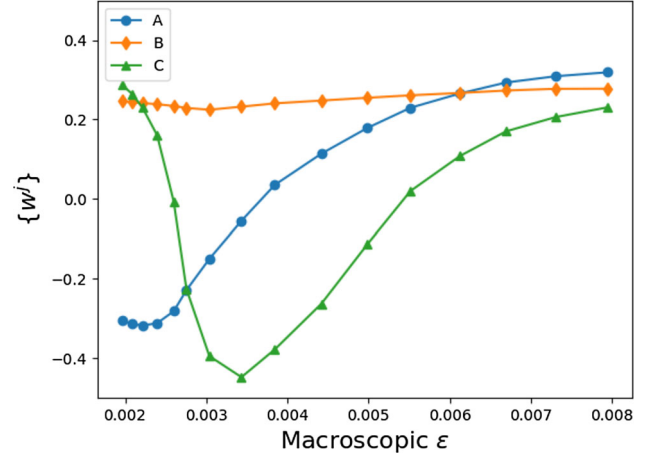


Fig. 3. The first three principal component vectors  $\{w^j\}$  plotted versus macroscopic strain  $\epsilon$ .

see in the figure that  $\{w^A\}$  rises to saturation,  $\{w^B\}$  is relatively constant, and  $\{w^C\}$  has a sharp oscillation downwards with a return to the initial value. The first three principal vectors appear to have analogues to mRSS behaviors at the elastic–plastic transition observed in the data, which will be reflected in the scores found when projecting the data against the principal vectors (noting the sign). A positive score found when projecting a mRSS history against  $\{w^A\}$  indicates a smooth work-hardening response, while a negative score indicates a smooth softening response. A mRSS history having a positive score when projected against  $\{w^C\}$  indicates a short softening transient, while a negative score indicates a work-hardening transient. Lastly, since  $\{w^B\}$  is relatively flat, large scores when projected against  $\{w^B\}$  indicate little evolution of the mRSS response once a grain has begun to yield. As the principal vectors can be interpreted as the vectors *closest* to the observation set,<sup>30</sup> in this case the mRSS histories, the resemblance to the stress behaviors is not unexpected.

The scores for the grain mRSS histories were calculated as described in the “Materials and Methods” section. Scatter plots of the data projected on to the principal component vectors are shown in Fig. 4a–c. There do not appear to be any trends in the principal component B and C scores ( $z^B$  versus  $z^C$ ). The clearest trends appear in Fig. 4b ( $z^A$  versus  $z^C$ ) where the data are concentrated on a relatively tight arc, which indicates that there appears to be a correlation between how much of a smooth stress evolution behavior ( $z^A$ ) and how much of a short transient is necessary ( $z^C$ ) to capture an observed mRSS response. Interestingly, both extreme ends of the curve have positive values of  $z^C$ , indicating a softening transient existing in the data. We can also see that these data appear to fall into four groups separated along  $z^A$ . K-Means clustering was used to separate these four groups using the  $z^A$ – $z^C$

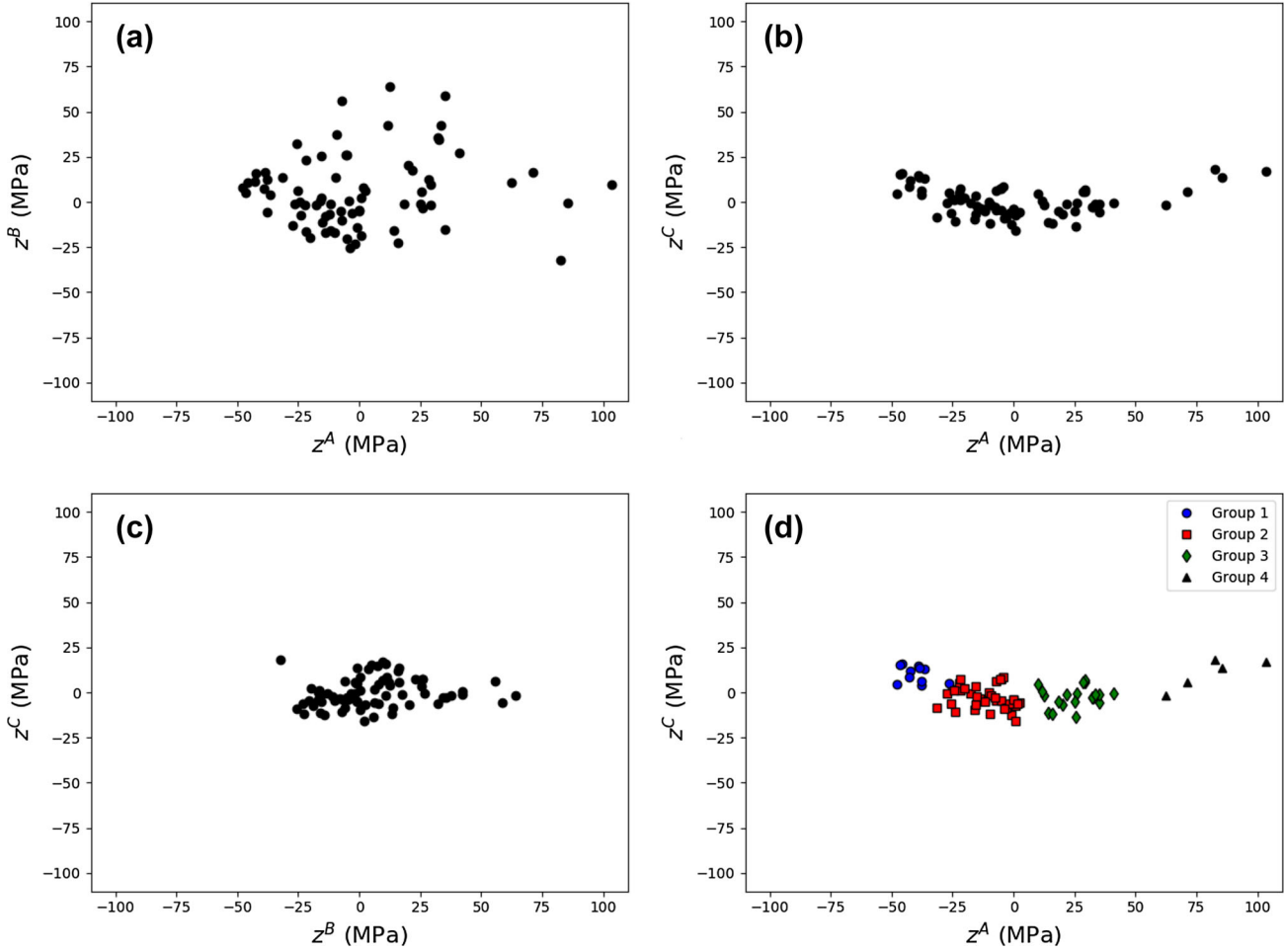


Fig. 4. (a) Scatter plot of  $z^A$  versus  $z^B$ . (b) Scatter plot of  $z^A$  versus  $z^C$ . (c) Scatter plot of  $z^B$  versus  $z^C$ . (d) Scatter plot of  $z^A$  versus  $z^C$  colored by groups found using K-Means clustering. Group 1 is blue, Group 2 is red, Group 3 is green, and Group 4 is black.

projection, and the groupings are shown in Fig. 4d. While four groups appear to be present, analysis of the K-Means objective found diminishing returns with the inclusions of more than four clusters. In the figure, blue corresponds to ‘Group 1’, red to ‘Group 2’, green to ‘Group 3’, and black to ‘Group 4’. These colors will be used to identify these groups for the rest of the paper. We note that the division of behavior is primarily through the  $z^A$  score (scores separated along  $z^A$ ), however, the  $z^A$ - $z^C$  projection provides clearer groupings.

The mRSS histories of the four groups are plotted in Fig. 5a–d. The average responses of each group of histories are also shown with a dashed line in the plots. As we see in the figure, the classification process readily divided the grains into different behavior sets. Group 1 histories correspond to grains that show the most (major) softening, consistent with the relatively large  $z^C$  scores. Grains in Group 2 show little work-hardening or -softening, consistent with the  $z^A$  and  $z^C$  scores near 0. Group 3 grains show moderate amounts of work-hardening which aligns well with the moderate and positive  $z^A$

scores and  $z^C$  scores near 0. Lastly, Group 4 grains show the most (major) work-hardening and have the largest  $z^A$ . These grains also have relatively large positive  $z^C$  scores, indicating that a short transient softening was necessary to capture the behavior of Group 4 grains.

## DISCUSSION

The evolution of the maximum resolved shear stress of grains in Al-Li 2099 was analyzed using unsupervised learning techniques. The PCA classified the grains into four groups: (1) major softening, (2) no work-hardening or -softening, (3) moderate work-hardening, and (4) major work-hardening. The unsupervised learning provided a more nuanced view of the behavior classification than a simple binary choice of hardening or softening,<sup>22</sup> providing a new means with which to quantitatively understand and classify constitutive response. As we better classify grain responses, we can improve our micromechanical models by ensuring that they include the most critical features of the deformation response. This is especially critical for modeling

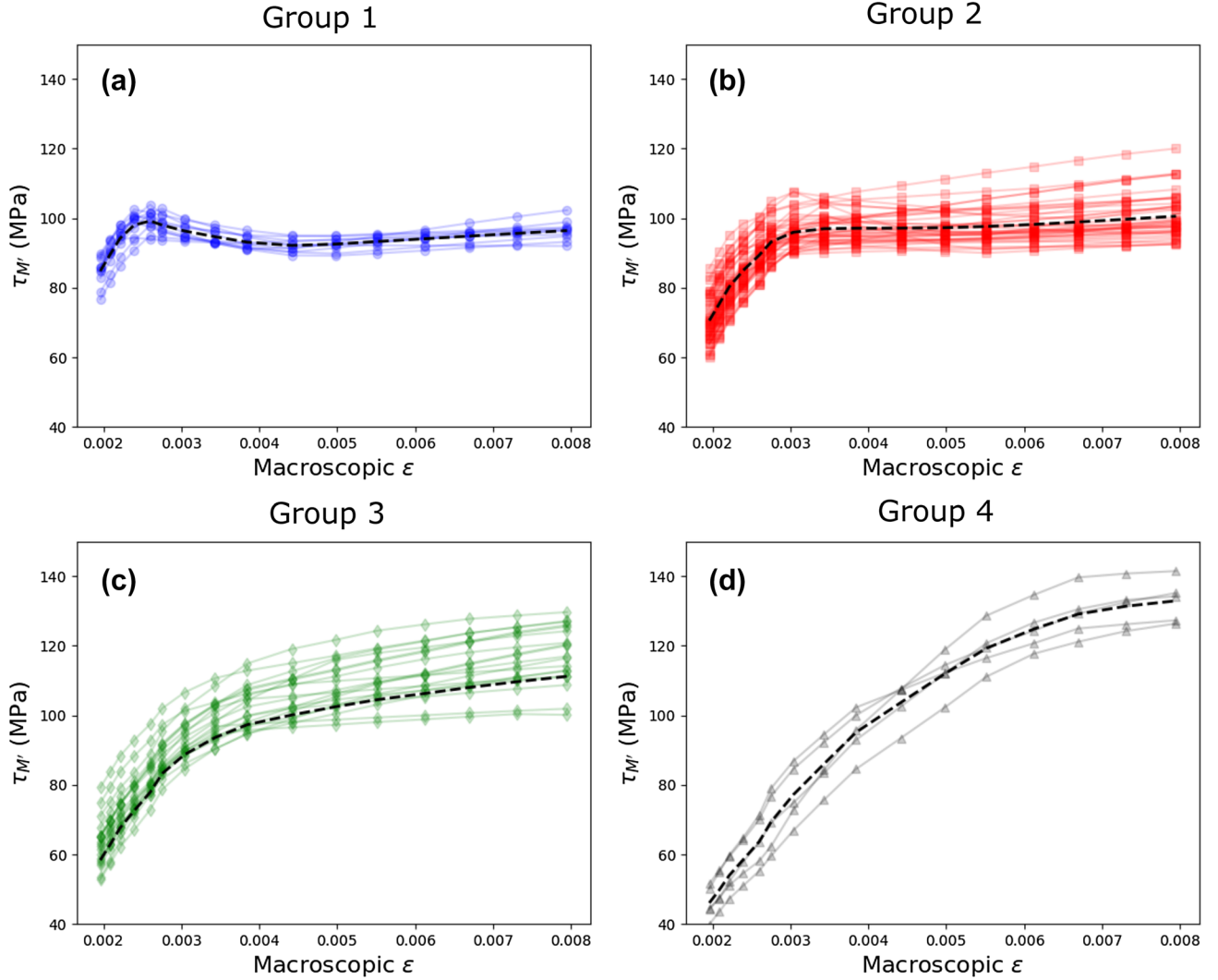


Fig. 5. Denoised mRSS histories ( $\tau_M$ ) of grains in (a) Group 1, (b) Group 2, (c) Group 3, and (d) Group 4. The dashed line shows the average response of each group.

complex processes such as strain localization, believed to be intimately tied to the initiation of fatigue and fracture, where multiple competing hardening and softening behaviors may be occurring simultaneously.

### Orientation and Spatial Dependence of Grain Behaviors

The orientation dependence of the mRSS response of these grains has been previously studied.<sup>22</sup> However, in light of the new behavior classifications found using PCA, it is worth revisiting Fig. 6a–c in more detail. Figure 6a shows the orientation of the loading axis for all grains on an inverse pole figure with each grain colored by the group label. Figure 6b and c color the grain-loading axis orientations by the principal vector A and C scores ( $z^A$  and  $z^C$ ), respectively. Generally, we see in Fig. 6b that  $z^A$ , correlated with long-transient hardening

behavior, has a strong orientation dependence. Conversely,  $z^C$  values in Fig. 6c, correlated with short-transient softening, does not have a strong orientation dependence.

The locations of both hardening grain groups (Groups 3 and 4) are near the edges of the triangle. Group 4 grains, which exhibited the most work-hardening, are located near [111] and are the most tightly co-located grains on the inverse pole figure (Fig. 6a). It has been well established that grains loaded along [111] in FCC metals often develop different microstructures in comparison to other orientations.<sup>31–33</sup> In a similar manner, the classification process appears to indicate that the hardening behavior is also markedly different than other orientations. Since Group 4 grains also have large  $z^A$  scores, the largest  $z^A$  scores are found near [111] as expected. Group 3 grains that showed moderate work-hardening are found near all three high-symmetry directions: [100], [110], and [111].

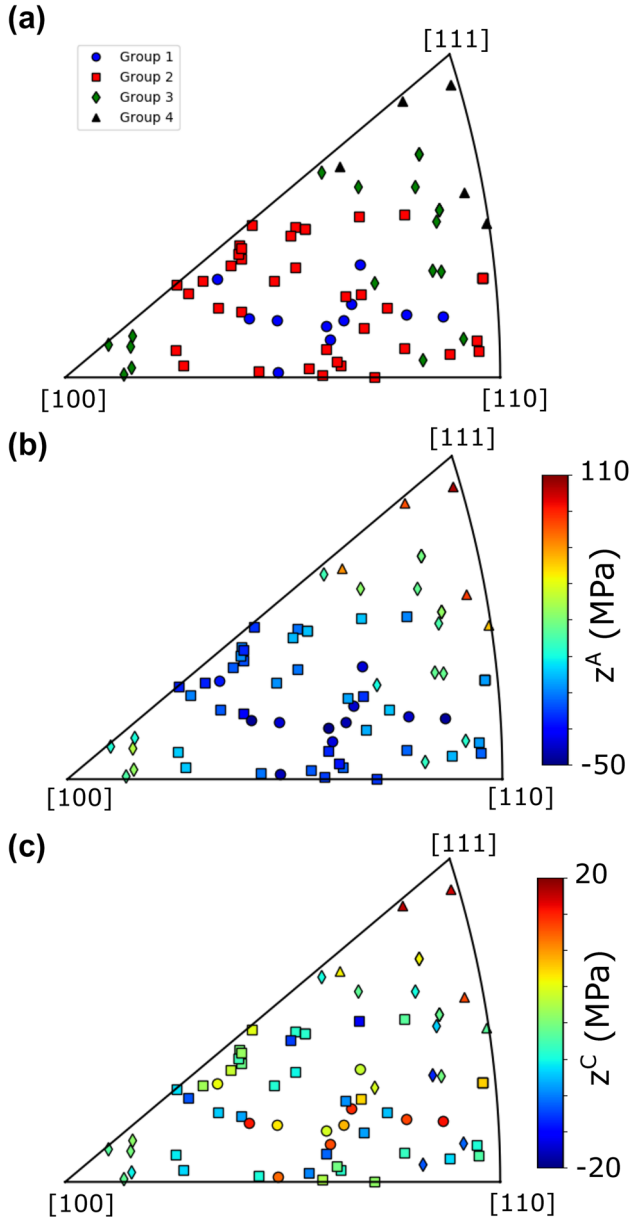


Fig. 6. Orientation of the loading axis for the grains studies plotted on inverse pole figures. (a) Loading axis orientations colored by group. (b) Loading axis orientations colored by principal component A score,  $z^A$ . (c) Loading axis orientations colored by principal component C score,  $z^C$ .

As these grains have a higher propensity for polyslip, slip system interactions are likely the cause of the observed work-hardening.

Both Group 1 and Group 2 grains are primarily located near the center of the triangle in Fig. 6a. In addition, there are grains in Groups 1 and 2 that have the loading axis near the high-symmetry [110] direction, but not near [111] or [100]. These two groups appear to be interspersed, and there is not a clear orientation dependence separating their behaviors. The interspersed nature of Groups 1 and 2 on the inverse pole figure indicates that another microstructural feature other than orientation

may be dictating the difference in behavior; this is also supported by Fig. 6c. Again, a large positive  $z^C$  score shows that a softening transient was in the mRSS response, and that there is little orientation dependence of these values. The spread of  $z^C$  also hints that softening may be more prevalent than initial inspection would suggest. Grains in all groups may show some amount of softening, but the behavior is masked and dominated by the work-hardening response (large  $z^A$ ). Therefore, the pronounced softening in Group 1 is likely the result of a microstructural feature not present in Group 2, in addition to minimal work-hardening. Critically, though, the present analysis appears to be able to deconvolute these behaviors.

Other microstructural features to investigate are the spatial position and size of grains in the sample. Figure 7 shows two views of the grain morphology measured using near-field HEDM colored by group (voxel spacing of  $5 \mu\text{m}$ ). The rolling direction (RD), transverse direction (TD), and normal direction (ND) of the plate from which the sample was cut are marked. Also, we note that faces normal to TD and ND are free surfaces and the sample was loaded along RD. By volume, Group 2 grains are most prevalent. In addition, Group 2 grains are on average about 10% larger than Group 1 grains (Group 1 mean volume:  $0.0126 \text{ mm}^3$  and Group 2 mean volume:  $0.0141 \text{ mm}^3$ ). However, no clear differences can be found between Groups 1 and 2. As no obvious spatial differences between Group 1 and 2 appear, the difference between these grains may exist at a lower length scale. More detailed microscopy studies may be able to conclusively determine the difference.

Grains in Groups 3 and 4 tend to be smaller than those in Groups 1 and 2. The mean volume of Group 3 grains is  $0.0083 \text{ mm}^3$  and the mean volume of Group 4 grains is  $0.0120 \text{ mm}^3$ . The observation that grains with behavior dominated by softening, and planar slip, being larger in our analysis (in this case, Groups 1 and 2) aligns with previous work.<sup>34</sup> However, the ability to project measured stress directly on to slip systems in situ and analyze the data with unsupervised learning have demonstrated that, in addition to grain size, grain orientation and hardening behavior due to slip system interactions are critical for interpreting grain deformation behavior.

### Applying Training to Other Samples

To explore the robustness of the classification process, another set of mRSS histories from a second sample (S2) that was loaded in the same manner (uniaxial tension with a displacement rate of  $10 \text{ nm/s}$ ) as the primary sample (S1) was analyzed. The mRSS histories were scored using Eq. 4 and principal component vectors found from S1. Used in this manner, S1 data were used as ‘training

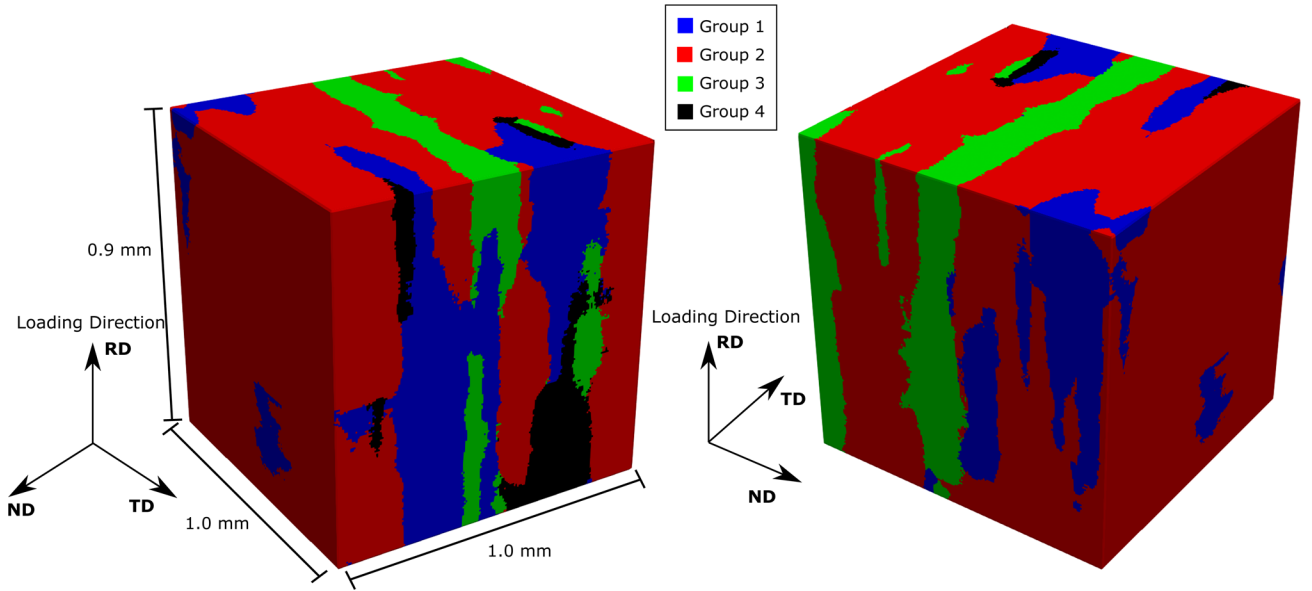


Fig. 7. Two views of the grain morphology in the sample studied colored by group.

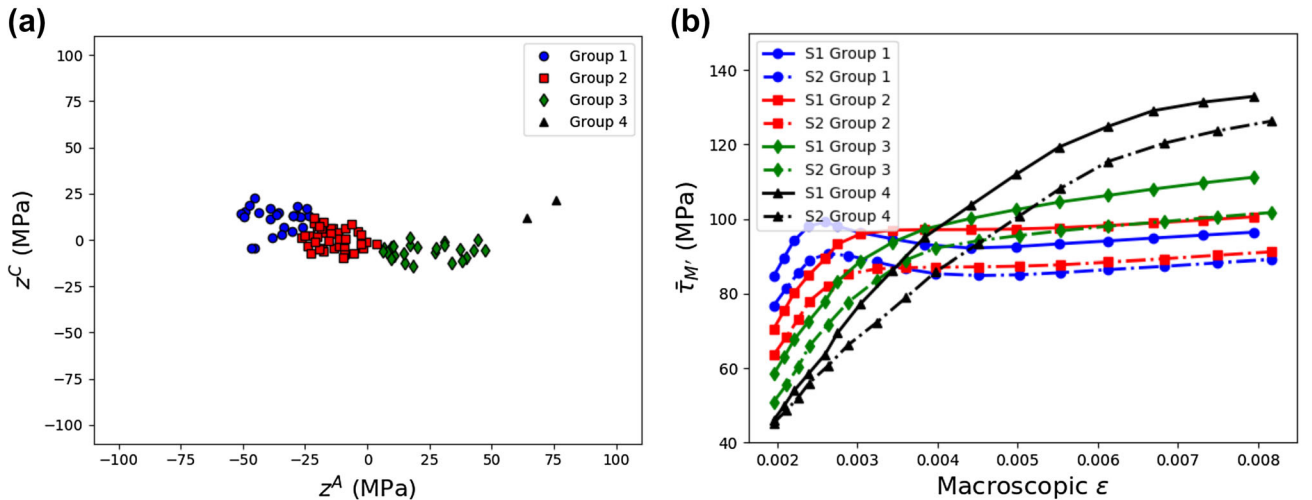


Fig. 8. (a) Scatter plot of  $z^A$  versus  $z^C$  colored by groups found using K-Means clustering in Sample 2 (S2). (b) Comparison of average mRSS histories  $\bar{\tau}_M$  from the 4 groups in the primary sample analyzed (S1, solid lines) and Sample 2 (S2, dash-dotted lines).

data' for fitting the principal component projection pre-processing step, which was then 'tested' on the S2 data. The first three principal component vectors found from S1 data explain 98.5% of the data variance in S2. The  $z^A$  and  $z^C$  scores from S2 are plotted in Fig. 8a and colored by group. We see that the four groups of stress histories in roughly the same location on the  $z^A$ - $z^C$  projection were found in S2. This finding shows that the four behaviors identified were not specific to a single sample. To emphasize this, Fig. 8b shows the average responses  $\bar{\tau}_M$  from the four grain behavior groups in the two samples. In both samples, Group 1 corresponds to major softening, Group 2 to no work-hardening or -softening, Group 3 to moderate work-

hardening, and Group 4 to major work-hardening. The repeatability of the classification analysis helps to provide confidence in the generality of the conclusions in this work.

## SUMMARY

A new unsupervised learning method for classifying measured grain stress behaviors was presented. The method was applied to HEDM data measured in situ from Al-Li 2099 deformed in uniaxial tension. The automated process divided the grain behaviors into four distinct groups. The classification process indicated that grains with the [111] direction aligned with the tensile axis hardened in a distinctly different manner than all other

grains. Also, grain stress softening behavior at yield appears to be prevalent in more grains than initially believed and correlated to a heterogeneous microstructural feature other than orientation.

### ACKNOWLEDGEMENT

This work is based upon research conducted at the Cornell High Energy Synchrotron Source (CHESS) which is supported by the National Science Foundation under Award DMR-1332208.

### REFERENCES

1. A. Tatzschl, and O. Kolednik, *Mater. Sci. Eng. A* (2003).
2. T. Turner, P. Shade, J. Schuren, and M. Groeber, *Modell. Simul. Mater. Sci. Eng.* 21 015002 (2012).
3. A. D. Kammers, and S. Daly, *Exp. Mech.* 53 1743 (2013).
4. H. Poulsen, *Three-Dimension X-Ray Diffraction Microscopy*, 1st edn. (Berlin: Springer, 2004).
5. L. Margulies, T. Lorentzen, H. Poulsen, and T. Leffers, *Acta Mater.* 50 1771 (2002).
6. U. Lienert, M. Brandes, J. Bernier, J. Weiss, S. Shastri, M. Mills, and M. Miller, *Mater. Sci. Eng. A* 524, 46 (2009).
7. T. R. Bieler, L. Wang, A. J. Beaudoin, P. Kenesei, and U. Lienert, *Metall. Mater. Trans. A* 45 109 (2013).
8. A. Beaudoin, M. Obstalecki, W. Tayon, M. Hernquist, R. Mudrock, P. Kenesei, and U. Lienert, *Acta Mater.* 61 3456 (2013).
9. M. Obstalecki, S.-L. Wong, P. Dawson, and M. Miller, *Acta Mater.* 75 259 (2014).
10. J. Oddershede, S. Schmidt, H. F. Poulsen, L. Margulies, J. Wright, M. Moscicki, W. Reimers, and G. Winther, *Mater. Charact.* 62 651 (2011).
11. H. Abdolvand, M. Majkut, J. Oddershede, S. Schmidt, U. Lienert, B. J. Diak, P. J. Withers, and M. R. Daymond, *Int. J. Plast.* 70 77 (2015).
12. D. C. Pagan, P. A. Shade, N. R. Barton, J.-S. Park, P. Kenesei, D. B. Menasche, and J. V. Bernier, *Acta Mater.* 128 406 (2017).
13. D. M. Dimiduk, E. A. Holm, and S. R. Niezgodza, *IMMI* 7 157 (2018).
14. V. Sundararaghavan, and N. Zabarar, *Stat. Anal. Data Min. ASA Data Sci. J.* 1 306 (2009).
15. S. R. Kalidindi, S. R. Niezgodza, G. Landi, S. Vachhani, and T. Fast, *CMC* 17 103 (2010).
16. S. R. Niezgodza, A. K. Kanjarla, and S. R. Kalidindi, *IMMI* 2 3 (2013).
17. N. H. Paulson, M. W. Priddy, D. L. McDowell, and S. R. Kalidindi, *Acta Mater.* 129 428 (2017).
18. S. K. Jha, R. A. Brockman, R. M. Hoffman, V. Sinha, A. L. Pilchak, W. J. Porter, D. J. Buchanan, J. M. Larsen, and R. John, *JOM* 70 1147 (2018).
19. A. J. Beaudoin, P. A. Shade, J. C. Schuren, T. J. Turner, C. Woodward, J. V. Bernier, S. F. Li, D. M. Dimiduk, P. Kenesei, and J.-S. Park, *Phys. Rev. B* 96 174116 (2017).
20. A. Mangal, and E. A. Holm, *Int. J. Plast.* 111 122 (2018).
21. A. Mangal, and E. A. Holm, *Int. J. Plast.* 114 1 (2019).
22. W. A. Tayon, K. E. Nygren, R. E. Crooks, and D. C. Pagan, *Acta Mater.* 173 231 (2019).
23. T. Sanders, and E. Starke, *Acta Metall.* 30 927 (1982).
24. P. Bate, Y. Huang, and F. Humphreys, *Acta Mater.* 52 4281 (2004).
25. N. Y. Juul, G. Winther, D. Dale, M. K. Koker, P. Shade, and J. Oddershede, *Scr. Mater.* 120 1 (2016).
26. D. C. Pagan, J. V. Bernier, D. Dale, J. P. Ko, T. J. Turner, B. Blank, and P. A. Shade, *Scr. Mater.* 142 96 (2018).
27. J. Bernier, N. Barton, U. Lienert, and M. Miller, *J. Strain Anal. Eng. Des.* 46 527 (2011).
28. P. Rodriguez, B. Wohlberg, *IEEE Trans. Imag. Proc.* 18 322 (2009).
29. R. Chartrand, and B. Wohlberg, Total-variation regularization with bound constraints, in *2010 IEEE International Conference on Acoustics, Speech and Signal Processing (IEEE, 2010)*, p. 766.
30. G. James, D. Witten, T. Hastie, and R. Tibshirani, *An introduction to statistical learning*, vol. 112 (New York: Springer, 2013).
31. P. Ambrosi, E. Göttler, and C. Schwink, *Scr. Metall.* 8 1093 (1974).
32. X. Huang, A. Borrego, and W. Pantleon, *Mater. Sci. Eng. A* **237**, 319–321 (2001).
33. N. Hansen, X. Huang, and G. Winther, *Metall. Mater. Trans. A* 42 613 (2011).
34. A. A. Csontos, and E. A. Starke, *Int. J. Plast.* 21 1097 (2005).

**Publisher's Note** Springer Nature remains neutral with regard to jurisdictional claims in published maps and institutional affiliations.